APPLIED PHYSICS

Reactive reconstruction and embedded passivation of heterointerfaces for intrinsically stable perovskite photovoltaics

Zhixin Ren[1]†, Jike Ding[2]†, Yuan Qiu[1], Huanqi Cao[1]*, Cong Chen[2,3]*, Shifu Zhang[1], Ulrich Wilhelm Paetzold[4], Jinzhao Li[4,5]*, Qian Zhao[1], Liying Yang[1], Shougen Yin[1]*, Jijian Lian[6]*

Heterointerface degradation under operational stress represents a critical limitation to perovskite solar cell longevity. Here, we demonstrate contrasting aging behaviors between bulky anionic and cationic passivators at heterointerfaces, wherein anionic species induce lattice expansion under thermal stress. To address the thermal instability of conventional passivators, we synthesized cesium pyridine-3-carboxylate, which triggers reactive surface reconstruction, suppresses ion migration, and enhances interfacial charge transfer. Devices using this passivation strategy achieved certified power conversion efficiencies of 27.28% with exceptional operational stability. Unencapsulated devices retained 87% of their initial efficiency after 4092 hours of maximum power point tracking under the ISOS-L-1 protocol, while encapsulated devices maintained 80% of their initial efficiency after 3566 hours at 85°C under the ISOS-L-2 protocol. These findings establish rational design principles for stabilizing perovskite heterointerfaces and advancing device durability.

INTRODUCTION

The evolution of organic-inorganic hybrid perovskite solar cell (PSC) has been noteworthy, with power conversion efficiency (PCE) exceeding 27% (*1*), making them a leading candidate for next-generation photovoltaic technology. High-efficiency PSCs are fabricated with procedures incorporating interface passivation, which is pivotal in enhancing their performance and stability. However, achieving intrinsically stable PSCs still remains a challenge for the successful commercialization of the technology.

To achieve intrinsically stable PSCs, various strategies have been explored, such as composition engineering (*2*–*5*), additive engineering (*1*, *6*–*9*), facet engineering (*10*–*12*), and interfacial engineering (*13*–*17*). Interfacial engineering with passivators has been used as a routine method, with the passivators including alkylammonium halides that can form two-dimensional (2D)/3D heterojunctions (*18*–*21*), Lewis acid-base materials that can be matched with defects (*22*–*24*), and polymers or inorganics that can act as barrier layers (*25*–*27*). Nevertheless, even if device performance and stability are enhanced via interfacial passivation, adverse factors may appear that trigger catastrophic device degradation (*1*, *18*, *28*–*30*). In particular, under operational stress, structural degradation at heterointerfaces can induce energy level mismatch and exacerbate ion migration. Studies in the literature have mostly focused on charge transport loss and recombination loss at the interfaces. In contrast, the structural evolution of the passivated heterointerfaces under operational stress has received limited attention, yet it is of great importance for understanding and elucidating the stability of photovoltaic devices under practical operating conditions.

We compared the effect of passivators with either cationic or anionic passivating groups, including phenylethylammonium iodide (PEAI), phenylethylammonium pyridine-3-carboxylate (PEAP3C), cesium acetate (CsAc), cesium pyridine-2-carboxylate (CsP2C), CsP3C, and CsP4C. Among them, CsP3C derived from vitamin B3 was found to be most effective for posttreatment of perovskite surfaces. We identified different functions between anionic and cationic passivating groups on perovskite and established that anions substantially enhance the stability by intercalating the lattice. This anion-embedment strategy induces reactive reconstruction, which homogenizes the surface morphology, reduces surface vacancy defects, inhibits the escape of volatile components, and even suppresses ion migration. We also demonstrated that this passivator is not only applicable to perovskites prepared by various methods but also compatible with both solution and vapor passivation techniques, exhibiting universality of the strategy. High efficiency was thus achieved with this strategy, with a certified steady-state PCE of 27.28% on small-area PSCs and 22.75% on perovskite solar modules (PSMs). Meanwhile, devices demonstrate exceptional photothermal stability under the International Summit on Organic Photovoltaic Stability (ISOS) protocols (*31*). Furthermore, these findings offer insights into bulky anion engineering, highlighting its potential for addressing key stability challenges in perovskite optoelectronics.

RESULTS

Structural evolution of heterointerfaces under thermal stress

Ionic polarity of the passivating group determines structural stability of the interface of perovskites. Three passivators were chosen,

[1]Key Laboratory of Display Materials and Photoelectric Devices (Ministry of Education), Tianjin Key Laboratory for Photoelectric Materials and Devices & National Demonstration Center for Experimental Function Materials Education, School of Materials Science and Engineering, Tianjin University of Technology, Tianjin 300384, P.R. China. [2]State Key Laboratory of Intelligent Power Distribution Equipment and System, School of Materials Science and Engineering, Hebei University of Technology, Tianjin 300401, P.R. China. [3]Macao Institute of Materials Science and Engineering (MIMSE), Faculty of Innovation Engineering, Macau University of Science and Technology, Taipa, Macao 999078, P.R. China. [4]Institute of Microstructure Technology, Karlsruhe Institute of Technology, Engesserstrasse 13, 76131 Karlsruhe, Germany. [5]State Power Investment Corporation Research Institute, Beijing 102209, P.R. China. [6]Marine Energy and Intelligent Construction Research Institute, Tianjin University of Technology, Tianjin 300384, P.R. China.
*Corresponding author. Email: caoh@tjut.edu.cn (H.C.); chencong@hebut.edu.cn (C.C.); lijinzhao@spic.com.cn (J. Li); sgyin@tjut.edu.cn (S.Y.); jjlian@tju.edu.cn (J. Lian)
†These authors contributed equally to this work.

including PEAI, PEAP3C, and CsP3C (Fig. 1A), representing bulky cation, bulky cation and anion, and bulky anion passivators, respectively.

The chemical structure of CsP3C was confirmed by ^{1}H nuclear magnetic resonance (^{1}H NMR; fig. S1). In CsP3C-treated perovskite films (target), the x-ray diffraction (XRD) peak of PbI_2 was greatly attenuated, whereas the peak of perovskites remained unaltered, implying CsP3C predominantly eliminated unreacted PbI_2 but generated no new phases (Fig. 1B and fig. S2). This finding was confirmed by incidence-angle (α)–dependent grazing incidence wide-angle x-ray scattering (GIWAXS; figs. S3 and S4).

Besides, CsP3C treatment greatly improves thermal stability of perovskites, as confirmed by photoluminescence (PL) spectra and XRD (Fig. 1C and figs. S5 and S6). PL intensity of the PEAI-treated film degraded to 59% of its initial value after 480 hours' aging at 85°C, while the CsP3C-treated film retained 89% of its initial value after thermal aging. Confocal fluorescence microscopy revealed the same tendency (fig. S7). These results demonstrate that CsP3C can sustain stable surface under thermal stress, by ways of suppressing halide/cation migration and volatilization of decomposed species (Fig. 1B).

To further investigate the origin of the notably improved thermal stability, we subjected perovskites treated with the above three types of passivators to operational stress at 85°C, during which they were traced with GIWAXS at a fixed α of 0.3° (figs. S3 and S4), where crystalline information of the surface 43 nm was detected (fig. S8). The 2D/3D heterojunction formed on the PEAI-treated film gradually disappeared during thermal aging, indicating a structural degradation (Fig. 1D) (*18*, *28*, *32*–*34*). In contrast, after thermal aging, the crystalline phase of the PEAP3C or CsP3C-treated samples remained unchanged, and their crystallinity in the surface region was even enhanced (Fig. 1E and fig. S9).

Azimuthal-angle (φ)–dependent GIWAXS analysis reveals strong correlation between the aged structure and polarity types of the passivator ions. The (100) reflection was chosen for analysis, with φ values of 10°, 90°, 130°, and 170° representing diffraction nearby the in-plane, out-of-plane, tilting, and in-plane directions, respectively.

After heating, for the PEAI-treated sample (Fig. 1, F and G, and fig. S10), its full widths at half maximum (FWHMs) gradually increased toward smaller α, indicating a reduction in crystalline domain size on the surface. In addition, the scattering vector gradually increased toward smaller α values, indicating that the surface layers experienced a triaxial compressive strain. Both can be attributed to that PEAI undergoes deprotonation under thermal stress and escapes from the surface, causing degradation of the 2D/3D heterojunctions.

However, an opposite phenomenon was observed on the CsP3C-treated sample (fig. S11). Its FWHM became narrower in the whole α range, and peak intensity was enhanced, indicating that its crystalline domain becomes larger. The scattering vector gradually decreased toward smaller α values, indicating that P3C anions intercalate the surface layers and a triaxial tensile strain was induced by the bulky P3C anion, which is larger than that of the matrix iodide anion. The nonvolatility of P3C under thermal stress endows the N atoms of pyridine capture protons detached from MA^+ or FA^+ under thermal stress (fig. S12), forming a strongly bound ammonium-like complex that occupies A-site vacancies (*35*–*37*), passivating Frenkel-type defects via an embedment mechanism.

The PEAP3C-treated sample did not form 2D/3D heterojunctions, but its P3C anions also intercalated the perovskite phase during heating (fig. S13). To confirm that $P3C^-$ anions can be embedded in perovskite lattices, we also conducted φ-dependent GIWAXS analysis on reflections including (110; fig. S14), (111; fig. S15), and (200; fig. S16), all revealing the same tendency. The divergence unveils that the surface structure of perovskites is more influenced by the anions than cations of the passivators.

The embedment behavior of bulky P3C anions was verified via high-resolution transmission electron microscopy (HRTEM). Cross-sectional HRTEM images were taken from focused ion beam (FIB)–cut samples. From fast Fourier transform results on selected areas (Fig. 2A), it was determined that the control sample exhibited a perovskite phase at the $PC_{61}BM$/perovskite interface. In the target sample, however, reactive reconstruction between CsP3C and PbI_2 generates a passivation layer with a thickness of about 5 nm, rendering the perovskite surface uniform and smooth (fig. S17), which reduces direct contact between the metal electrode and the perovskite absorption layer, thereby addressing potential performance limitations and enhancing device stability (*38*).

After aging in a glove box for about 1 month, both control and target FIB-cut samples were reexamined. The control sample exhibited plenty of PbI_2 (fig. S18). An encouraging difference is that the target sample even maintained a perovskite phase after the long-term storage. The enhanced stability might be related with the lattice expansion induced by P3C anion and the nonvolatility of CsP3C (*2*, *39*, *40*). We further conjecture that the stability gains reported for $PO(OH)_2$-terminated self-assembled monolayers (SAMs) and related bulky anions arise at least, in part, from intercalation (*41*–*43*).

Homogenized surface and suppressed ionic migration

Scanning electron microscopy (SEM) and atomic force microscopy (AFM) images (Fig. 2C and figs. S20 to S22) confirm the presence of unreacted PbI_2 (bright clusters) at grain boundaries on the surface of the control perovskite film. As expected, these PbI_2 clusters were gradually removed upon CsP3C treatments, with roughness reduced and grain size increased (table S1). Similar tendency was observed on AFM phase distribution maps (fig. S23). Upon CsP3C treatments, the surface morphology becomes flattened. Meanwhile, Kelvin probe force microscopy (KPFM) measurements confirm that the work function is decreased and the surface potential becomes more homogeneous (fig. S22).

The CsP3C treatment reduced the trap-state density from 8.05×10^{15} to 4.46×10^{15} cm^{-3} (fig. S25), underscoring the favorable effects of reactive reconstruction and embedded passivation in reducing defect density and suppressing nonradiative recombination.

XRD measurements confirm the reaction between CsP3C and PbI_2 (fig. S25). For a molar ratio of 1: 1 (CsP3C: PbI_2), a transparent and amorphous phase was formed, while for 2: 1, the film still exhibited inappreciable absorption in the visible region, but a δ-$CsPbI_3$ phase was formed (*44*). P3C acid and PbI_2 did not react upon mixing, indicating that the reaction involves participation of Cs. The increase in entropy of the system upon amorphization (increase in grain boundary) could be offset by the reaction between CsP3C and PbI_2, endowing the possibility of surface reconstruction.

Activation energy (E_a) of ion migration was experimentally obtained from fitting of the low-frequency region of temperature-dependent Nyquist plots (fig. S28) (*45*–*47*). The E_a values in the control and target devices were 0.37 and 0.62 eV, respectively (Fig. 2D), indicating that the surface-reconstructed perovskites help suppress ion migration. The ion migration rates (k) of the control and target devices were estimated to be 7.4×10^7 and 9.4×10^3 s^{-1}, respectively,

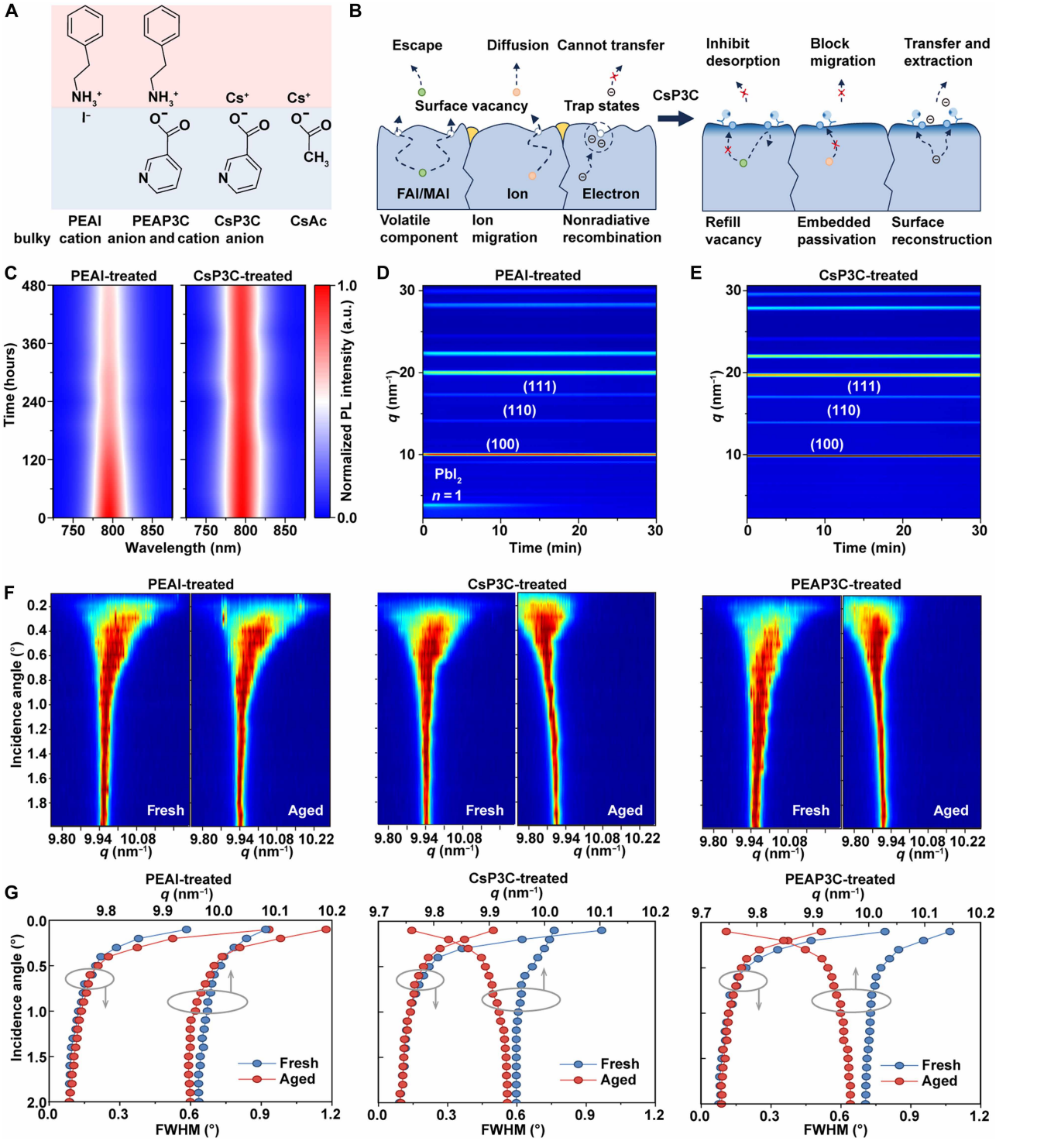

Fig. 1. Structural evolution of heterointerfaces during aging. (**A**) Molecular structures of CsP3C, PEAP3C, CsAc, and PEAI. (**B**) Schematic illustration of the effect of CsP3C treatments on perovskites. (**C**) Photoluminescence (PL) spectra repeatedly measured on PEAI-treated and CsP3C-treated films aging at 85°C. a.u., arbitrary units. (**D**) and (**E**) show in situ grazing incidence wide-angle x-ray scattering (GIWAXS) results under annealing at 85°C with a fixed incident angle of 0.3°. (**F**) The azimuthally incidence-angle (φ)–dependent GIWAXS results for CsP3C-, PEAP3C-, and PEAI-treated perovskite films, respectively, before and after aging at 85°C. (**G**) The variation of full width at half maximum (FWHM) and center vector before and after aging at 85°C.

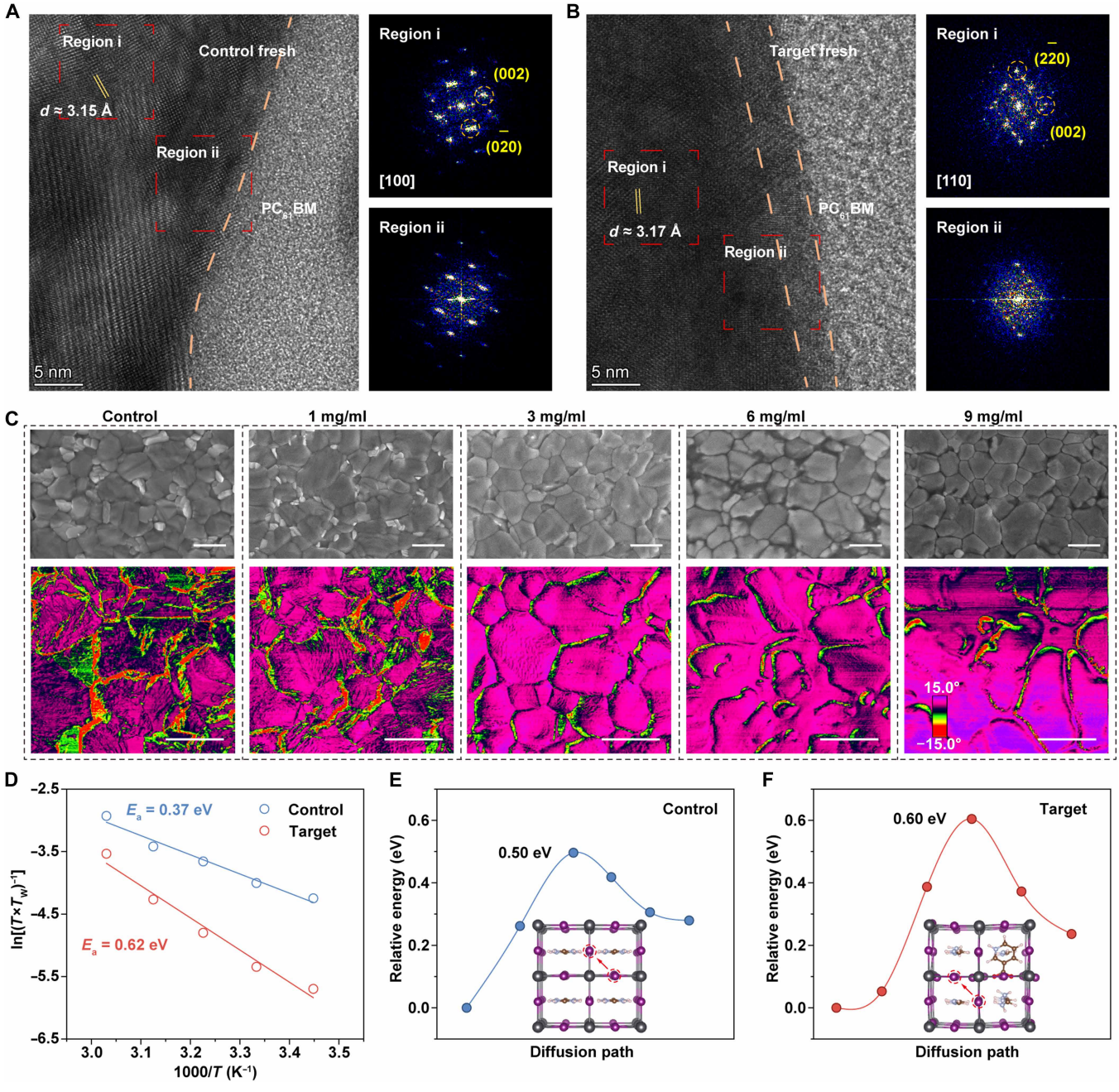

Fig. 2. Micro impacts on heterointerfaces. (**A** and **B**) HRTEM results of the control and the target samples taken on whole devices. (**C**) Top-view scanning electron microscopy (SEM) images (top) and atomic force microscopy (AFM) phase distribution images (bottom) of perovskite films were treated with CsP3C at different concentrations. Scale bars, 1 μm. (**D**) Activation energy derived by Arrhenius-like plot of impedance for control and target-based devices. (**E** and **F**) Density functional theory (DFT)–calculated activation energy for I migration in $FAPbI_3$ and P3C-substituted $FAPbI_3$ perovskites, respectively. The inset presents the crystal structures and migration pathways.

a four order-of-magnitude decrease after CsP3C treatment, confirming that ionic diffusion was largely suppressed.

To deeper understand the interaction between CsP3C and perovskites, we carried out theoretical calculation with density functional theory (DFT) on models with Frenkel-type defects, i.e., FA and iodine (I) vacancies (fig. S29). When the surface vacancies are occupied by CsP3C molecules, with Cs^+ fill the A-site vacancies and $P3C^-$ anion fill the X-site vacancies, the energy of the system is lowered by 2.7 eV per passivator molecule. Upon surface adsorption, the meta-site nitrogen atom on the pyridine ring of P3C strongly donates electrons to defects on the perovskite surface, and P3C forms a negative electropotential together with Pb cations compared to the I anions, which is favorable to the charge extraction at the interface.

When the defect occurred in the bulk, the energy of the system is lowered by 2.4 eV per passivator molecule. Notably, calculations also suggest that P3C doping has negligible impact on the electronic

structure of perovskites (fig. S30). The migration barrier for iodide anions in perovskites with a climbing image nudged elastic band (CI-NEB) method: an iodide anion migrated from its initial position to a neighboring vacancy site (V_I) along the shortest path in the [110] direction (migration path shown in Fig. 2, E and F). The results indicate that after P3CA passivates nearby defects, the perovskite exhibits a higher iodide ion migration barrier (0.60 eV) compared to the control sample (0.50 eV). This confirms that P3C-containing perovskites exhibit suppressed I^- migration compared to pure $FAPbI_3$.

Transient carrier behaviors

Ultrafast transient absorption (TA) spectroscopy was used to compare carrier transfer and recombination kinetics. The samples exhibited TA valleys centered at 763 nm (Fig. 3, A and D), originating from the occupation of excited charge states by pump photons. The increase in lifetime τ_1 in the CsP3C-treated sample indicates the suppressed recombination of excited carriers in the bulk. The increase in τ_2, on the other hand, suggests longer diffusion lifetime of carriers toward surface in the film.

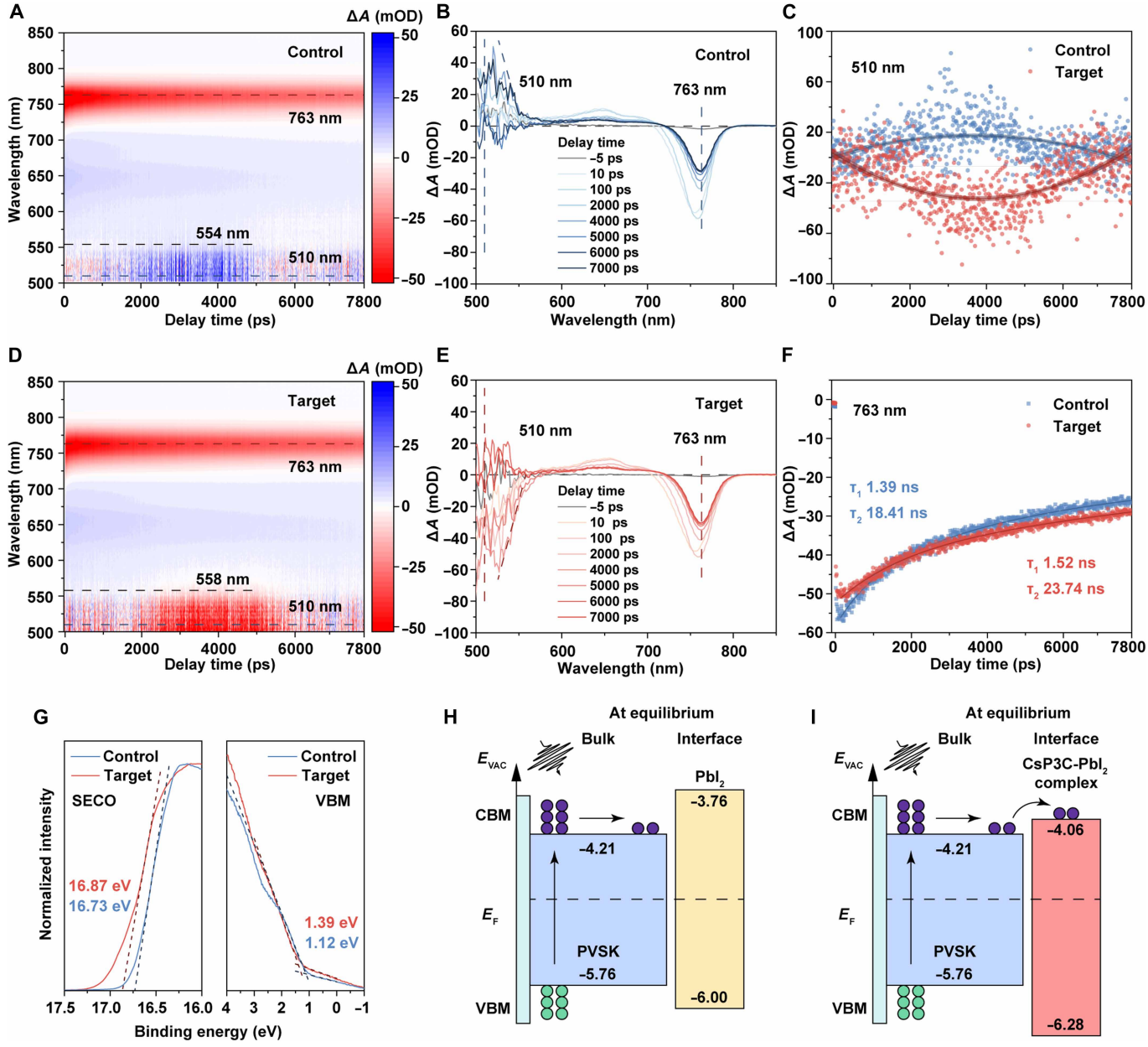

Fig. 3. Carrier behavior of perovskite films. (**A** and **D**) The 2D color representation of TA spectral evolution for the control (A) and target (D) perovskite films. Color bar, differential optical density, in milli-optical density (mOD). (**B** and **E**) TA spectra of the control and target perovskite films were measured at different probe delay times. (**C** and **F**) TA kinetics of the control and target perovskite films were probed at selected wavelengths. (**G**) Ultraviolet photoelectron spectra (UPS) around the secondary electron cutoff (SECO, left) and in the valence band maximum (VBM, right) region. (**H** and **I**) Schematic carrier energy level diagrams illustrating the changes after Fermi level flattening. PVSK, perovskite.

For the untreated film (Fig. 3A), a TA peak was observed around 510 nm, associated with the deoccupation of excited states in remanent PbI_2 phases. In contrast, a TA valley around 510 nm was observed in the treated film (Fig. 3D), suggesting the reoccupation of excited states in PbI_2-related species. On the basis of the corresponding absorption edges, bandgaps of PbI_2-related phases in untreated and treated samples were determined to be 2.24 and 2.22 eV, respectively. Combined these results with ultraviolet photoelectron spectra (UPS; Fig. 3G), we conjecture that the CsP3C treatment successfully reduced conduction band offset (CBO) at the interface (Fig. 3, H and I, and fig. S31) (*48*). This optimized type-I band alignment, with a reduced CBO, simultaneously facilitates carrier transport and suppresses charge recombination (*49*). Enhanced PL intensity and PL/TA lifetimes confirm the effectively suppressed nonradiative recombination in the treated sample (fig. S32 and table S3).

Meanwhile, transient photovoltage (TPV; fig. S33) and transient photocurrent (TPC; fig. S33) measurements demonstrate prolonged carrier recombination lifetime and shorter carrier transport time. These results also indicate reduced nonradiative recombination at the interfaces of the CsP3C-treated device, as well as faster charge transport and extraction (*50*).

Enhancement of photovoltaic properties

We assessed the photovoltaic performance of PSCs with a p-i-n configuration: glass/indium tin oxide (ITO)/NiO_x/Me-4PACz/perovskite/passivation layer/$PC_{61}BM$/BCP/Ag or Cu (Fig. 4A), with the perovskite layer processed with various methods and passivated with PEAI, PEAP3C, CsAc, CsP2C, CsP3C, or CsP4C (figs. S34 to S37 and tables S4 and S5). Among them, CsP3C demonstrated the best passivation effect. The concentration of CsP3C was optimized at 3.0 mg ml^{-1} (Fig. 4B, fig. S38, and table S6). The PCE of champion target devices was 26.03 and 25.85% (by antisolvent, reverse and forward scans, respectively) and 27.41 and 27.37% (by vacuum-flash, reverse and forward scans, respectively), with negligible hysteresis. In contrast, the PCE of the optimal control device was 23.76 and 23.71% (by antisolvent, reverse and forward scans, respectively) and 25.17 and 25.12% (by vacuum-flash, reverse and forward scans, respectively) (table S7). We submitted our champion devices to an accredited third-party institution for independent certification. The certified steady-state PCE was 27.28% (fig. S39).

Meanwhile, we also fabricated PSMs with an aperture area of 16.41 cm^2 (Fig. 4C), achieving a PCE of 22.75% with a geometric fill factor (GFF) of 96.4%. These results confirm the scalability of this strategy for large-scale applications. Besides spin coating, the thermally stable anion-based passivator is also compatible with vapor processing (Fig. 4D, fig. S40, and table S8) (*51*, *52*), further underscoring the versatility and practicality of the approach. Furthermore, as indicated by the corresponding external quantum efficiency (EQE) spectra, the reduction in Urbach energy of the target device suggests mitigated band-edge disorder (fig. S41).

Stability of devices was investigated according to ISOS protocols. The operational stability of unencapsulated control and target devices was tracked at the maximum power point (MPP) under 1-sun illumination in ambient air (ISOS-L-1). The target device retained 87% of the initial PCE after aging for 4092 hours (Fig. 4E), in comparison to 22% efficiency retention for the control device. We further evaluated the photothermal stability of encapsulated control and target devices at 85°C and 1-sun illumination under open-circuit condition (ISOS-L-2). The T_{80} lifetime (time for 80% efficiency retention) reached 3566 hours for the CsP3C-treated device (Fig. 4, F and G), representing excellent thermal stability among reported PSCs (detailed stability metrics in table S9).

J-V curve tracing during MPP tracking (MPPT) revealed that FF values of the CsP3C-treated device only decreased slightly during the whole photothermal aging, whereas the control device exhibited pronounced FF degradation (Fig. 4, G and H). The robust FF indicates that stability of the heterointerfaces in the device has been greatly improved after CsP3C treatment. The outstanding thermal stability can be attributed to the continuous stabilization effect played by the embedded passivator at the heterointerfaces.

DISCUSSION

In this work, we observed contrasting aging behaviors between bulky anionic versus cationic passivators at the interface. A reactive reconstruction and embedded passivation strategy are demonstrated on the basis of bulky anion passivators. The intrinsically thermal stable CsP3C is not only applicable to perovskites prepared by various methods but also compatible with vapor passivation techniques. Owing to the strong reaction between CsP3C and PbI_2, recrystallization of imperfect perovskite surface became thermodynamically feasible, which homogenizes the surface. This process reduces vacancy defects, inhibits the escape of volatile components, and suppresses ionic migration. Furthermore, it effectively promotes charge transfer and extraction. These features promote the stable operation of devices under operational stresses. Our findings provide deep insights into enhancing the stability of perovskites under practical working conditions. Meanwhile, the diffusion behavior of other common passivators at heterointerfaces under harsh operational stress remains poorly understood, warranting further in-depth exploration.

MATERIALS AND METHODS

Materials

All the materials are used as received without further purification. Commercial indium tin oxide (ITO) substrates (15 ohm/square) were purchased from Liaoning Yike Precision. MAI (methylammonium iodide), FAI (formamidinium iodide), and MACl (methylammonium chloride) were purchased from Great Cell Solar. PbI_2 and Me-4PACz were purchased from TCI. CsI (cesium iodide), *N*,*N*′-dimethylformamide (DMF), and dimethyl sulfoxide (DMSO) were purchased from Sigma-Aldrich. $PC_{61}BM$ and BCP were purchased from Hanfeng Chemical. (4-(7H-dibenzo[c,g]carbazol-7-yl)butyl) phosphonic acid (4PADBC) was purchased from Xi'an Yuri Solar Corp. NiO_x was purchased from Xi'an Elight Corp. Pyridine-2-carboxylic acid (P2CA), P3CA, and P4CA were purchased from TCI. Isopropyl alcohol (IPA), Cs_2CO_3 and β-phenylethylamine were purchased from J&K Scientific. All other materials and solvents were purchased from J&K Scientific.

Preparation of PEAP3C and CsP3C: The PEAP3C or CsP3C powders were synthesized by mixing P3CA and β-phenylethylamine or Cs_2CO_3, respectively, into deionized water under 80°C for 4 hours. Other salts were prepared in a similar manner. For further purification, these powders were recrystallized three times with methanol. The product powders were collected by vacuum filtration. Last, the PEAP3C and CsP3C were dried for 8 hours in a vacuum drying oven at 80°C to remove the solvent.

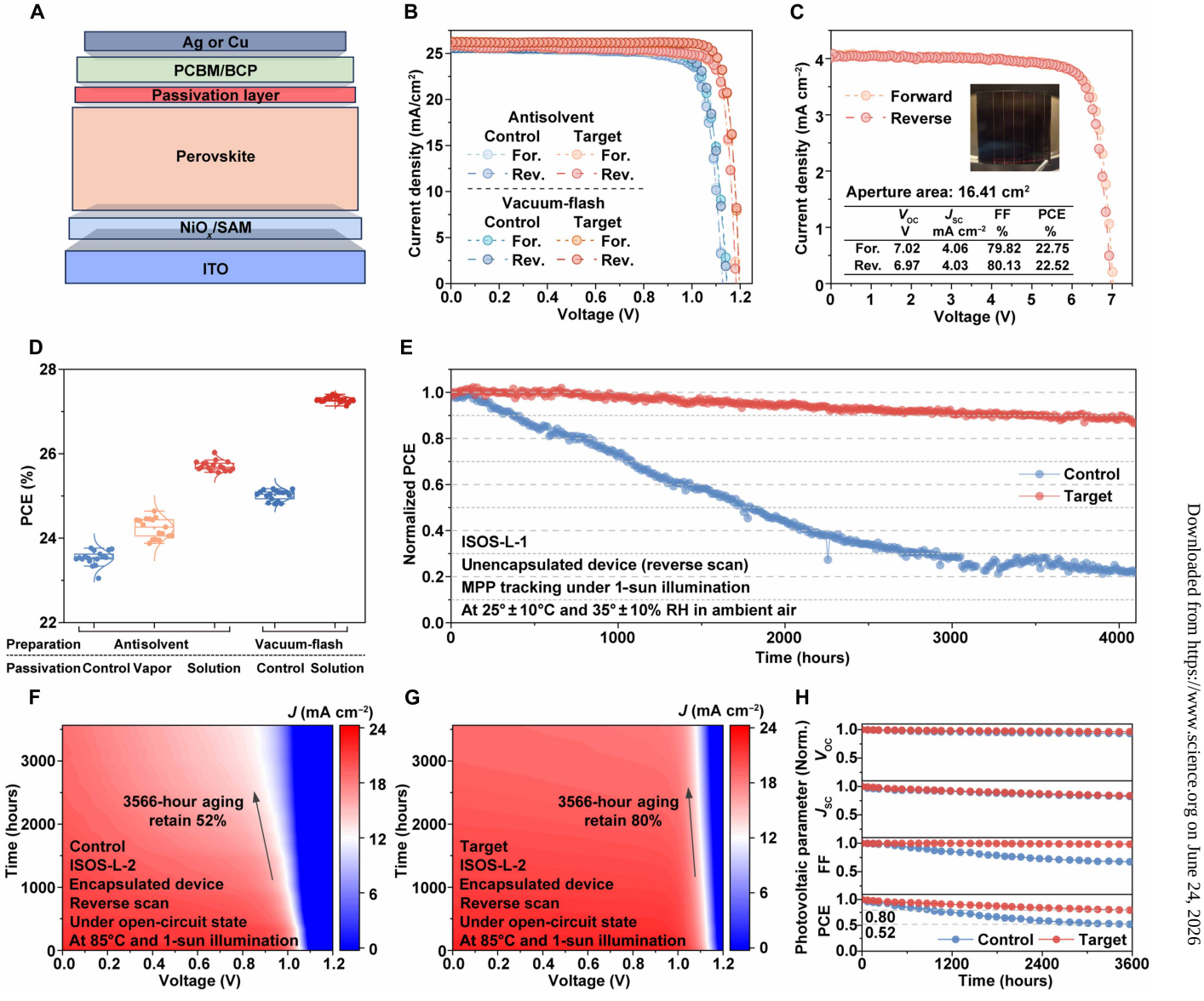

Fig. 4. Device structure and photovoltaic performance. (**A**) Device structure of PSCs. (**B**) *J-V* curves with forward and reverse scans of the control and target devices fabricated via the antisolvent and vacuum-flash methods, respectively. For., forward; Rev., reverse. (**C**) *J-V* curves with forward and reverse scans of CsP3C-passivated modules. (**D**) Box plots of photovoltaic parameters for CsP3C-passivated devices via vapor and solution passivation methods. (**E**) Maximum power point tracking (MPPT) for the unencapsulated control and target devices under 1-sun illumination in ambient air (ISOS-L-1). RH, relative humidity. (**F** and **G**) *J-V* curves of the encapsulated control and target devices measured following ISOS-L-2. (**H**) Normalized parameters of encapsulated devices aging at 85°C and 1-sun illumination under open circuit (ISOS-L-2). Norm., normalized.

Device fabrication

The PSC configuration is glass/ITO/NiO_x/Me-4PACz/perovskite/passivation layers/$PC_{61}BM$/BCP/Cu. First, glass/ITO substrates were sequentially cleaned by cleaning agent, deionized water, and ethanol, each for 20 min in an ultrasonic bath. Before use, the ITO was cleaned with ultraviolet ozone for 20 min to remove any residual contamination. Thin layers of NiO_x were fabricated by spin coating NiO_x nanoparticle ink onto the cleaned ITO at 4000 rpm for 30 s, followed by annealing at 150°C for 10 min. Then, the substrates were transferred into a nitrogen glovebox. Me-4PACz (0.5 mg ml^{-1} in IPA) was spin coated onto the NiO_x surface at 4000 rpm for 30 s, followed by annealing at 100°C for 10 min. Then, 1.5 M perovskite precursor solutions were constructed by mixing CsI, MAI, FAI, and PbI_2 in 1 ml of anhydrous DMF:DMSO mixed solvent [4:1 (v/v)] with the chemical formula $Cs_{0.1}MA_{0.05}FA_{0.85}PbI_3$ with 9 mol % PbI_2 excess. Then, 15 mol % MACl was added to the precursor solution. Afterward, the precursor solution was shaken on a stirring hot plate set to 60°C for 2 hours. The prepared precursor solutions were filtered before use. The perovskite layer was spin coated with a two-step method, first at 1000 rpm for 10 s, followed by 5000 rpm for 40 s. In the second step, anhydrous anisole (300 μl) was dripped onto the substrate as a continuous droplet 10 s before the end of the second

step. The substrate was immediately placed on a hot plate and annealed at 110°C for 30 min. The best efficiency was optimized through the flash evaporation process.

The best efficiency was optimized through the flash evaporation process. The stoichiometric $Cs_{0.05}FA_{0.95}PbI_3$ precursor solution was prepared by dissolving 19.5 mg of CsI, 245.1 mg of FAI, 12 mg of MACl, and 726.1 mg of PbI_2 in mixed solvents of DMF/DMSO (630 μl/157 μl). For the 1.54-eV $Cs_{0.05}FA_{0.95}PbI_3$ film crystallization, the perovskite film was deposited by spin coating the perovskite precursor solution on glass/F-doped tin oxide (FTO)/4PADBC substrate at 1000 rpm for 10 s and 3000 rpm for 30 s. Specifically, the wet perovskite film was quickly put into a sample chamber connected to vacuum-pumping instrumentation (internal space is 12 cm by 12 cm by 2.1 cm). By opening the valve connecting the specimen chamber to the pump system, the perovskite film was immediately exposed to low pressure maintained at 10 Pa for 38 s, followed by full pressurization by admitting ambient air into the specimen chamber. Subsequently, the perovskite film was annealed at 102°C for 35 min in the N_2 for full crystallization. Our vacuum-flash evaporation setup uses an Edwards mechanical pump with a pumping speed of 4 liters s^{-1}. After transferring the sample from the spin coater to the vacuum-flash evaporation chamber, we switch on the vacuum-flash evaporation system; the chamber pressure drops from ambient [~1 atm (101.325 kPa)] to <10 Pa within 2 to 3 s. This rapid pumpdown is essential. Moreover, our results and experience show that, whether performed in ambient air or in a N_2 glovebox, the rapid initial crystallization of evaporating solvents proceeds without participation of air (or only with a negligible amount), which is why the process can be reliably carried out in air.

For the surface treatment, the passivating solutions were prepared by dissolving various passivators in IPA. Passivation layers were fabricated by depositing the passivating solution (100 μl) onto the perovskite film surface, and after deposition, the film was spin coated at 4000 rpm for 30 s. The films were then annealed at 100°C for 5 min. Then, $PC_{61}BM$ (20 mg ml^{-1} in chlorobenzene) was spin coated at 2000 rpm for 30 s, followed by a 10-min annealing at 100°C. After letting the substrates to cool for 5 min, BCP (0.5 mg ml^{-1} in IPA) was spin coated at 4000 rpm for 30 s, with a 5-min annealing at 70°C. Last, 100 nm of Ag was thermally evaporated (under a vacuum $< 5.0 \times 10^{-4}$ Pa) to produce a cell with an active area of 0.075 cm^2. For stability tests, SnO_x is used instead of BCP, and Cu is used instead of Ag. A 20-nm-thick SnO_x layer deposited by atomic layer deposition (ALD) was used as buffer layer. The substrate temperature was maintained at 80°C during ALD deposition with Tetrakis(dimethylamino)tin(IV) (TDMASn) precursor source at 60°C and H_2O source at room temperature. With a 50–standard cubic centimeter per minute N_2, the pulse and purge times for TDMASn are 0.1 and 60.0 s, respectively, while for H_2O is 0.6 and 60.0 s, respectively. A total of 140 cycles was used.

Module fabrication

Compared with the fabrication of each functional layer of a small-area solar cell, except for the corresponding increase in the amount of solution, other parameters remain unchanged. A perovskite module with six-series subcells was fabricated on a 5 cm–by–5 cm glass/ITO substrate with a P1 channel. A 15-nm-thick SnO_x layer was deposited by ALD using 110 cycles. After P2, a 10-nm-thick SnO_x layer was redeposited as interdiffusion barrier using 70 cycles. Subsequently, 100 nm of Cu was thermally evaporated. Last, the P3 was mechanically scribed. The widths of P1, P2, and P3 are 30, 80, and 30 μm, respectively. The width of safe zone is 50 μm. P2 was etched using a picosecond green laser (532 nm, 6 W, power of 3.4%, 1000 kHz). P3 was etched using a picosecond green laser (532 nm, 6 W, power of 12%, 2000 kHz). The GFF is 96.4%.

Space charge limiting current device fabrication

Space charge limiting current (SCLC) measurement was obtained using electron-only (ITO/SnO_2/perovskite/PCBM/Ag) devices. In the case of electron-only devices, the substrate was spin coated with a thin layer of SnO_2 nanoparticle solution (1:6; SnO_2 [15% in water]: water) at 3000 rpm for 20 s and annealed in ambient air at 150°C for 0.5 hours. For SCLC devices, the preparation method of the perovskite and that of the identical functional layer are consistent with those described above.

Characterizations

Device measurements

The *J-V* curves and MPPT data were recorded using a programmed Keithley 2400 source meter in combination with a hermetic sample holder (PURI Materials). The measurements were conducted under the illumination provided by a solar simulator (Newport, AM1.5G, with an intensity of 100 mW cm^{-2}). For the scan process, a reverse scan from 1.3 to −0.2 V and a forward scan from −0.2 to 1.3 V were performed, both with a step size of 20 mV and a delay of 500 ms per step. The light source of the solar simulator was calibrated in advance using a standard monocrystalline silicon solar cell (SRC-1000TC-QZ, VLSI Standards Inc.). EQE spectra were acquired using a programmed Keithley 2400 source meter. The process involved passing the output of a 15-W Xenon lamp through a monochromator to enable the measurement. SCLC measurements were measured by the Keithley 2400 source meter under dark conditions. All the measurements were performed in Ar. For the ISOS-L-1 aging tests, MPPT is recorded by the aging light source test system (SS-L16X and LS6000 software, ENLITECH). For the ISOS-L-2 aging test, the encapsulated device is placed under a solar simulator (MT-PV_16) with the temperature maintained at 85°C, and the *J-V* curve is measured at intervals. For our encapsulation, we use industry-compatible materials. First, ribbons are soldered to the electrodes of the devices to extend the connections. The device is encapsulated between two glasses and two layers of polyolefin elastomer (POE) encapsulation films (PHOTOCAP 6048, H.B. Fuller Company). We use edge sealant (HelioSeal PVS 101, H.B. Fuller Company) to prevent moisture ingress from the sides of the device. The stack is laminated in a hot press at 120°C for 20 min. All processes were done in ambient air.

Morphology characterization

For cross-sectional TEM measurements, ultrathin films were prepared first using a FIB–electron beam DualBeam equipment FIB-SEM system (Helios NanoLab 460HP, FEI). The samples were protected by electron beam and ion beam deposition of carbon and platinum layers, respectively. The bulk of the sample was milled and separated with the ion beam (30 kV and 6.5 nA), and the nanomanipulator lifted the sheet off and placed it on the TEM copper grid. The samples were thinned by reducing the FIB current (30 kV and 0.79 nA to 40 pA), and lastly, the cleaning work was carried out at 2 kV and 41 pA to remove any possible contamination of the samples. The HRTEM (Talos F200X) is equipped with an energy-dispersive x-ray and high-angle annular dark field (HAADF) detector in scanning TEM mode for imaging and elemental mapping at 300-kV operating voltage. The planar and

cross-sectional morphologies of thin films were characterized by SEM (SU8010, Hitachi; the voltage was 5 kV, and the current was 7 μA). The surface morphology, phases, and potential of perovskite films were measured using AFM with a tapping mode (Innova SPM, Bruker, Dimension Icon). The surface potentials of the films were characterized via KPFM integrating with the AFM system.

XRD, GIWAXS, x-ray photoelectron spectroscopy, and UPS measurements

XRD patterns were tested by a Rigaku SmartLab (9 kW) XRD with Cu Kα radiation. GIWAXS measurement was conducted at the mySpot beamline of the BESSY II facility at the Helmholtz-Zentrum Berlin (*53*). The measurement was performed with an x-ray energy of 9 keV. A focused x-ray beam, having a size of 100 μm by 100 μm, was directed onto the perovskite samples at an Anton Paar DHS 1100 domed heating stage. The incidence angles of the beam were varied from 0.1° to 2°, which was done to adjust the penetration depth of the x-rays into the samples. The diffraction patterns were collected using an Eiger 9M detector. For each incidence angle, the integration time for collecting the data was set to 20 s. The raw patterns were analyzed by pyFAI (*54*). X-ray photoelectron spectroscopy and UPS were carried out by Thermo Fisher Scientific, ESCALAB 250 Xi, Al Kα.

NMR, Fourier transform infrared, and thermogravimetric measurements

NMR was performed using Bruker Avance III 400 with a frequency of 400 MHz and deuterated DMSO as a solvent. Fourier transform infrared (FTIR) was measured by FTIR spectrometer (Frontier Mid-IR FTIR/STA6000-TL9000-Clarus SQ8). Thermogravimetry (TG) was measured by a thermalgravimetric analyzer (NETZSCH 209F3A).

TA spectroscopy

The measurements were conducted by the HARPIA-TA spectroscopy system, which is a part of the HARPIA system (HARPIA, Light Conversion). The light source of HARPIA-TA is a femtosecond laser (PH2-10W, Light Conversion; 290 fs to 10 ps, 1 Hz to 200 kHz) operating at 1030 nm. The fundamental laser is split into two beams. One is used to pump an optical parametric amplifier (OPA) system (ORPHEUS, Light Conversion), and the output of the OPA is used as a pump light of HARPIA-TA. The other one is used to generate supercontinuum white light that is further used as the probe light for differential absorption measurements. The white-light probe beam was achieved by focusing a portion of the laser output onto a sapphire crystal within the HARPIA spectrometer. The probe was time delayed with respect to the pump by a mechanical delay stage. Data were initially collected using the HARPIA-TA spectrometer and analyzed using CarpetView software (Light Conversion).

Ultraviolet-visible absorbance and PL measurement

The absorption spectra were tested using an ultraviolet-visible spectrophotometer (U-4100, Hitachi). PL and time-resolved photoluminescence (TRPL) spectra were tested using an Edinburgh FS5 spectrofluorometer. PL tracking was adopted as in literature (*55*). The excitation light is the 475-nm-wavelength light of a Xenon lamp (150 W, OSRAM), with an excitation intensity of about 0.3 mW cm^{-2} on the sample surface. PL lifetime mapping was tested by a time-resolved confocal fluorescence microscope imager (PicoQuant, MicroTime 200), with a 440-nm picosecond pulsed laser head selected for excitation.

Electrochemical impedance spectroscopy measurement

E_a was obtained by temperature-dependent electrochemical impedance spectroscopy of perovskite (*45*–*47*). By combining a vacuum cryogenic device with Zahner photoelectrochemical workstation, the device impedance at different temperatures was measured by applying an ac voltage under a light intensity of 100 mW cm^{-2}.

Other measurements

TPC decay and TPV decay were recorded by PD-RS of ENLITECH.

Simulation and calculation

The adsorption/binding energy and migration barrier were computed via DFT with DS-PAW software integrated in Device Studio. The electron-ion interactions were characterized via the projector augmented-wave (PAW) method. For the exchange-correlation functionals, the general gradient approximation with the Perdew-Burke-Ernzerhof functional was adopted. The (100) slab model of $FAPbI_3$ perovskite was built upon a cubic-phase primitive cell, comprising a $2 \times 2 \times 3$ supercell with a vacuum layer of no less than 15 Å along the z axis. In the slab model calculations, a plane-wave expansion energy cutoff of 500 eV and a k-point mesh of $2 \times 2 \times 1$ were used. The density of states of the bulk perovskite models was calculated with the inclusion of spin-orbit coupling. For the assessment of diffusion energy barriers of I vacancies, the CI-NEB method was implemented using the DS-PAW software.

Supplementary Materials

This PDF file includes:

Figs. S1 to S41
Tables S1 to S9
References

REFERENCES

1. Z. Xiong, Q. Zhang, K. Cai, H. Zhou, Q. Song, Z. Han, S. Kang, Y. Li, Q. Jiang, X. Zhang, J. You, Homogenized chlorine distribution for >27% power conversion efficiency in perovskite solar cells. *Science* **390**, 638–642 (2025).
2. S. Liu, Y. Lu, C. Yu, J. Li, R. Luo, R. Guo, H. Liang, X. Jia, X. Guo, Y.-D. Wang, Q. Zhou, X. Wang, S. Yang, M. Sui, P. Müller-Buschbaum, Y. Hou, Triple-junction solar cells with cyanate in ultrawide-bandgap perovskites. *Nature* **628**, 306–312 (2024).
3. E. Ugur, A. A. Said, P. Dally, S. Zhang, C. E. Petoukhoff, D. Rosas-Villalva, S. Zhumagali, B. K. Yildirim, A. Razzaq, S. Sarwade, A. Yazmaciyan, D. Baran, F. Laquai, C. Deger, I. Yavuz, T. G. Allen, E. Aydin, S. De Wolf, Enhanced cation interaction in perovskites for efficient tandem solar cells with silicon. *Science* **385**, 533–538 (2024).
4. J. Xu, C. C. Boyd, Z. J. Yu, A. F. Palmstrom, D. J. Witter, B. W. Larson, R. M. France, J. Werner, S. P. Harvey, E. J. Wolf, W. Weigand, S. Manzoor, M. F. A. M. Van Hest, J. J. Berry, J. M. Luther, Z. C. Holman, M. D. McGehee, Triple-halide wide–band gap perovskites with suppressed phase segregation for efficient tandems. *Science* **367**, 1097–1104 (2020).
5. J.-P. Correa-Baena, Y. Luo, T. M. Brenner, J. Snaider, S. Sun, X. Li, M. A. Jensen, N. T. P. Hartono, L. Nienhaus, S. Wieghold, J. R. Poindexter, S. Wang, Y. S. Meng, T. Wang, B. Lai, M. V. Holt, Z. Cai, M. G. Bawendi, L. Huang, T. Buonassisi, D. P. Fenning, Homogenized halides and alkali cation segregation in alloyed organic-inorganic perovskites. *Science* **363**, 627–631 (2019).
6. S. Li, Y. Jiang, J. Xu, D. Wang, Z. Ding, T. Zhu, B. Chen, Y. Yang, M. Wei, R. Guo, Y. Hou, Y. Chen, C. Sun, K. Wei, S. M. H. Qaid, H. Lu, H. Tan, D. Di, J. Chen, M. Grätzel, E. H. Sargent, M. Yuan, High-efficiency and thermally stable FACsPbI3 perovskite photovoltaics. *Nature* **635**, 82–88 (2024).
7. H. Chen, C. Liu, J. Xu, A. Maxwell, W. Zhou, Y. Yang, Q. Zhou, A. S. R. Bati, H. Wan, Z. Wang, L. Zeng, J. Wang, P. Serles, Y. Liu, S. Teale, Y. Liu, M. I. Saidaminov, M. Li, N. Rolston, S. Hoogland, T. Filleter, M. G. Kanatzidis, B. Chen, Z. Ning, E. H. Sargent, Improved charge extraction in inverted perovskite solar cells with dual-site-binding ligands. *Science* **384**, 189–193 (2024).
8. Z. Liang, Y. Zhang, H. Xu, W. Chen, B. Liu, J. Zhang, H. Zhang, Z. Wang, D.-H. Kang, J. Zeng, X. Gao, Q. Wang, H. Hu, H. Zhou, X. Cai, X. Tian, P. Reiss, B. Xu, T. Kirchartz, Z. Xiao, S. Dai, N.-G. Park, J. Ye, X. Pan, Homogenizing out-of-plane cation composition in perovskite solar cells. *Nature* **624**, 557–563 (2023).
9. P. Shi, Y. Ding, B. Ding, Q. Xing, T. Kodalle, C. M. Sutter-Fella, I. Yavuz, C. Yao, W. Fan, J. Xu, Y. Tian, D. Gu, K. Zhao, S. Tan, X. Zhang, L. Yao, P. J. Dyson, J. L. Slack, D. Yang, J. Xue, M. K. Nazeeruddin, Y. Yang, R. Wang, Oriented nucleation in formamidinium perovskite for photovoltaics. *Nature* **620**, 323–327 (2023).
10. C. Ma, F. T. Eickemeyer, S.-H. Lee, D.-H. Kang, S. J. Kwon, M. Grätzel, N.-G. Park, Unveiling facet-dependent degradation and facet engineering for stable perovskite solar cells. *Science* **379**, 173–178 (2023).

11. C. Ma, M.-C. Kang, S.-H. Lee, S. J. Kwon, H.-W. Cha, C.-W. Yang, N.-G. Park, Photovoltaically top-performing perovskite crystal facets. *Joule* **6**, 2626–2643 (2022).
12. C. Ma, M.-C. Kang, S.-H. Lee, Y. Zhang, D.-H. Kang, W. Yang, P. Zhao, S.-W. Kim, S. J. Kwon, C.-W. Yang, Y. Yang, N.-G. Park, Facet-dependent passivation for efficient perovskite solar cells. *J. Am. Chem. Soc.* **145**, 24349–24357 (2023).
13. O. Er-raji, C. Messmer, R. R. Pradhan, O. Fischer, V. Hnapovskyi, S. Kosar, M. Marengo, M. List, J. Faisst, J. P. Jurado, O. Matiash, H. P. Pasanen, A. Prasetio, B. Vishal, S. Zhumagali, A. R. Pininti, Y. Gupta, C. Baretzky, E. Ugur, C. E. Petoukhoff, M. Bivour, E. Aydin, R. Azmi, J. Schön, F. Schindler, M. C. Schubert, U. Schwingenschlögl, F. Laquai, A. A. Said, J. Borchert, P. S. C. Schulze, S. De Wolf, S. W. Glunz, Electron accumulation across the perovskite layer enhances tandem solar cells with textured silicon. *Science* **390**, eadx1745 (2025).
14. J. Liu, Y. He, L. Ding, H. Zhang, Q. Li, L. Jia, J. Yu, T. W. Lau, M. Li, Y. Qin, X. Gu, F. Zhang, Q. Li, Y. Yang, S. Zhao, X. Wu, J. Liu, T. Liu, Y. Gao, Y. Wang, X. Dong, H. Chen, P. Li, T. Zhou, M. Yang, X. Ru, F. Peng, S. Yin, M. Qu, D. Zhao, Z. Zhao, M. Li, P. Guo, H. Yan, C. Xiao, P. Xiao, J. Yin, X. Zhang, Z. Li, B. He, X. Xu, Perovskite/silicon tandem solar cells with bilayer interface passivation. *Nature* **635**, 596–603 (2024).
15. Y. Yang, H. Chen, C. Liu, J. Xu, C. Huang, C. D. Malliakas, H. Wan, A. S. R. Bati, Z. Wang, R. P. Reynolds, I. W. Gilley, S. Kitade, T. E. Wiggins, S. Zeiske, S. Suragtkhuu, M. Batmunkh, L. X. Chen, B. Chen, M. G. Kanatzidis, E. H. Sargent, Amidination of ligands for chemical and field-effect passivation stabilizes perovskite solar cells. *Science* **386**, 898–902 (2024).
16. C. Liu, Y. Yang, H. Chen, J. Xu, A. Liu, A. S. R. Bati, H. Zhu, L. Grater, S. S. Hadke, C. Huang, V. K. Sangwan, T. Cai, D. Shin, L. X. Chen, M. C. Hersam, C. A. Mirkin, B. Chen, M. G. Kanatzidis, E. H. Sargent, Bimolecularly passivated interface enables efficient and stable inverted perovskite solar cells. *Science* **382**, 810–815 (2023).
17. S. Mariotti, E. Köhnen, F. Scheler, K. Sveinbjörnsson, L. Zimmermann, M. Piot, F. Yang, B. Li, J. Warby, A. Musiienko, D. Menzel, F. Lang, S. Keßler, I. Levine, D. Mantione, A. Al-Ashouri, M. S. Härtel, K. Xu, A. Cruz, J. Kurpiers, P. Wagner, H. Köbler, J. Li, A. Magomedov, D. Mecerreyes, E. Unger, A. Abate, M. Stolterfoht, B. Stannowski, R. Schlatmann, L. Korte, S. Albrecht, Interface engineering for high-performance, triple-halide perovskite–silicon tandem solar cells. *Science* **381**, 63–69 (2023).
18. S. Tan, M.-C. Shih, Y. Lu, S.-G. Choi, Y. Dong, J.-H. Lee, I. Yavuz, B. W. Larson, S. Y. Park, T. Kodalle, R. Zhang, M. J. Grotevent, Y.-K. Lin, H. Zhu, V. Bulović, C. M. Sutter-Fella, N.-G. Park, M. C. Beard, J.-W. Lee, K. Zhu, M. G. Bawendi, Spontaneous formation of robust two-dimensional perovskite phases. *Science* **388**, 639–645 (2025).
19. R. Azmi, D. S. Utomo, B. Vishal, S. Zhumagali, P. Dally, A. M. Risqi, A. Prasetio, E. Ugur, F. Cao, I. F. Imran, A. A. Said, A. R. Pininti, A. S. Subbiah, E. Aydin, C. Xiao, S. I. Seok, S. De Wolf, Double-side 2D/3D heterojunctions for inverted perovskite solar cells. *Nature* **628**, 93–98 (2024).
20. R. Azmi, E. Ugur, A. Seitkhan, F. Aljamaan, A. S. Subbiah, J. Liu, G. T. Harrison, M. I. Nugraha, M. K. Eswaran, M. Babics, Y. Chen, F. Xu, T. G. Allen, A. U. Rehman, C.-L. Wang, T. D. Anthopoulos, U. Schwingenschlögl, M. De Bastiani, E. Aydin, S. De Wolf, Damp heat–stable perovskite solar cells with tailored-dimensionality 2D/3D heterojunctions. *Science* **376**, 73–77 (2022).
21. H. Chen, S. Teale, B. Chen, Y. Hou, L. Grater, T. Zhu, K. Bertens, S. M. Park, H. R. Atapattu, Y. Gao, M. Wei, A. K. Johnston, Q. Zhou, K. Xu, D. Yu, C. Han, T. Cui, E. H. Jung, C. Zhou, W. Zhou, A. H. Proppe, S. Hoogland, F. Laquai, T. Filleter, K. R. Graham, Z. Ning, E. H. Sargent, Quantum-size-tuned heterostructures enable efficient and stable inverted perovskite solar cells. *Nat. Photonics* **16**, 352–358 (2022).
22. Y. Ding, B. Ding, P. Shi, J. Romano-deGea, Y. Li, R. C. Turnell-Ritson, O. A. Syzgantseva, I. Yavuz, M. Xia, R. Yu, M. A. Syzgantseva, J.-N. Audinot, X. Miao, X. Liao, J. Li, P. Dörflinger, V. Dyakonov, C. Liu, Y. Yang, L. Tao, K. G. Brooks, A. Slonopas, J. Pan, L. Zhang, Q. An, Y. Rong, J. Peng, L. Ding, E. Shi, L. Mai, S. Dai, K. Zhao, J. Sheng, R. Wang, P. J. Dyson, M. K. Nazeeruddin, Cation reactivity inhibits perovskite degradation in efficient and stable solar modules. *Science* **386**, 531–538 (2024).
23. X. Ren, J. Wang, Y. Lin, Y. Wang, H. Xie, H. Huang, B. Yang, Y. Yan, Y. Gao, J. He, J. Huang, Y. Yuan, Mobile iodides capture for highly photolysis- and reverse-bias-stable perovskite solar cells. *Nat. Mater.* **23**, 810–817 (2024).
24. C. Li, X. Wang, E. Bi, F. Jiang, S. M. Park, Y. Li, L. Chen, Z. Wang, L. Zeng, H. Chen, Y. Liu, C. R. Grice, A. Abudulimu, J. Chung, Y. Xian, T. Zhu, H. Lai, B. Chen, R. J. Ellingson, F. Fu, D. S. Ginger, Z. Song, E. H. Sargent, Y. Yan, Rational design of Lewis base molecules for stable and efficient inverted perovskite solar cells. *Science* **379**, 690–694 (2023).
25. Q. Li, Y. Zheng, H. Wang, X. Liu, M. Lin, X. Sui, X. Leng, D. Liu, Z. Wei, M. Song, D. Li, H. G. Yang, S. Yang, Y. Hou, Graphene-polymer reinforcement of perovskite lattices for durable solar cells. *Science* **387**, 1069–1077 (2025).
26. P. Chen, Y. Xiao, J. Hu, S. Li, D. Luo, R. Su, P. Caprioglio, P. Kaienburg, X. Jia, N. Chen, J. Wu, Y. Sui, P. Tang, H. Yan, T. Huang, M. Yu, Q. Li, L. Zhao, C.-H. Hou, Y.-W. You, J.-J. Shyue, D. Wang, X. Li, Q. Zhao, Q. Gong, Z.-H. Lu, H. J. Snaith, R. Zhu, Multifunctional ytterbium oxide buffer for perovskite solar cells. *Nature* **625**, 516–522 (2024).
27. M. Xiao, G. Yuan, Z. Lu, J. Xia, D. Li, Y. Chen, Y. Zhang, F. Pei, C. Chen, Y. Bai, T. Song, J. Dou, Y. Li, Y. Chen, Z. Xu, X. Yang, Z. Liu, X. Liu, C. Zhu, Q. Chen, Engineering amorphous–crystallized interface of ZrN_x barriers for stable inverted perovskite solar cells. *Adv. Mater.* **35**, 2301684 (2023).
28. F. Pei, S. Lin, Z. Zhang, S. Lin, X. Huang, M. Zhao, J. Xu, X. Zhuang, Y. Zhang, J. Tang, Y. Chen, K. Li, L. Wang, G. Liu, D. Qian, H. Liu, W. Zhou, Y. Chen, J. Wang, H. Zhou, B. Li, D. Zhong, Y. Jiang, Q. Chen, Inhibiting defect passivation failure in perovskite for perovskite/Cu(In,Ga)Se2 monolithic tandem solar cells with certified efficiency 27.35%. *Nat. Energy* **10**, 824–835 (2025).
29. J. Xu, H. Chen, L. Grater, C. Liu, Y. Yang, S. Teale, A. Maxwell, S. Mahesh, H. Wan, Y. Chang, B. Chen, B. Rehl, S. M. Park, M. G. Kanatzidis, E. H. Sargent, Anion optimization for bifunctional surface passivation in perovskite solar cells. *Nat. Mater.* **22**, 1507–1514 (2023).
30. S. Tan, T. Huang, I. Yavuz, R. Wang, T. W. Yoon, M. Xu, Q. Xing, K. Park, D.-K. Lee, C.-H. Chen, R. Zheng, T. Yoon, Y. Zhao, H.-C. Wang, D. Meng, J. Xue, Y. J. Song, X. Pan, N.-G. Park, J.-W. Lee, Y. Yang, Stability-limiting heterointerfaces of perovskite photovoltaics. *Nature* **605**, 268–273 (2022).
31. M. V. Khenkin, E. A. Katz, A. Abate, G. Bardizza, J. J. Berry, C. Brabec, F. Brunetti, V. Bulović, Q. Burlingame, A. Di Carlo, R. Cheacharoen, Y.-B. Cheng, A. Colsmann, S. Cros, K. Domanski, M. Dusza, C. J. Fell, S. R. Forrest, Y. Galagan, D. Di Girolamo, M. Grätzel, A. Hagfeldt, E. Von Hauff, H. Hoppe, J. Kettle, H. Köbler, M. S. Leite, S. Liu, Y.-L. Loo, J. M. Luther, C.-Q. Ma, M. Madsen, M. Manceau, M. Matheron, M. McGehee, R. Meitzner, M. K. Nazeeruddin, A. F. Nogueira, Ç. Odabaşı, A. Osherov, N.-G. Park, M. O. Reese, F. De Rossi, M. Saliba, U. S. Schubert, H. J. Snaith, S. D. Stranks, W. Tress, P. A. Troshin, V. Turkovic, S. Veenstra, I. Visoly-Fisher, A. Walsh, T. Watson, H. Xie, R. Yıldırım, S. M. Zakeeruddin, K. Zhu, M. Lira-Cantu, Consensus statement for stability assessment and reporting for perovskite photovoltaics based on ISOS procedures. *Nat. Energy* **5**, 35–49 (2020).
32. C. Liu, Y. Yang, H. Chen, I. Spanopoulos, A. S. R. Bati, I. W. Gilley, J. Chen, A. Maxwell, B. Vishal, R. P. Reynolds, T. E. Wiggins, Z. Wang, C. Huang, J. Fletcher, Y. Liu, L. X. Chen, S. De Wolf, B. Chen, D. Zheng, T. J. Marks, A. Facchetti, E. H. Sargent, M. G. Kanatzidis, Two-dimensional perovskitoids enhance stability in perovskite solar cells. *Nature* **633**, 359–364 (2024).
33. M. Wang, Z. Shi, C. Fei, Z. J. D. Deng, G. Yang, S. P. Dunfield, D. P. Fenning, J. Huang, Ammonium cations with high pK_a in perovskite solar cells for improved high-temperature photostability. *Nat. Energy* **8**, 1229–1239 (2023).
34. C. A. R. Perini, E. Rojas-Gatjens, M. Ravello, A. Castro-Mendez, J. Hidalgo, Y. An, S. Kim, B. Lai, R. Li, C. Silva-Acuña, J. Correa-Baena, Interface reconstruction from Ruddlesden–Popper structures impacts stability in lead halide perovskite solar cells. *Adv. Mater.* **34**, 2204726 (2022).
35. X. Li, J. M. Hoffman, M. G. Kanatzidis, The 2D halide perovskite rulebook: How the spacer influences everything from the structure to optoelectronic device efficiency. *Chem. Rev.* **121**, 2230–2291 (2021).
36. X. Li, W. Ke, B. Traoré, P. Guo, I. Hadar, M. Kepenekian, J. Even, C. Katan, C. C. Stoumpos, R. D. Schaller, M. G. Kanatzidis, Two-dimensional Dion–Jacobson hybrid lead iodide perovskites with aromatic diammonium cations. *J. Am. Chem. Soc.* **141**, 12880–12890 (2019).
37. W. Li, X. Feng, K. Guo, W. Pan, M. Li, L. Liu, J. Song, Y. He, H. Wei, Prominent free charges tunneling through organic interlayer of 2D perovskites. *Adv. Mater.* **35**, 2211808 (2023).
38. H. Jin, M. D. Farrar, J. M. Ball, A. Dasgupta, P. Caprioglio, S. Narayanan, R. D. J. Oliver, F. M. Rombach, B. W. J. Putland, M. B. Johnston, H. J. Snaith, Alumina nanoparticle interfacial buffer layer for low-bandgap lead-tin perovskite solar cells. *Adv. Funct. Mater.* **33**, 2303012 (2023).
39. T. Lu, Z. Dang, Y. Luo, Y. Li, X. Rao, Z. Zhang, Y. Hu, Z. Chen, Z. Li, U. Petralanda, J. Xie, J. Yu, P. Gao, Lattice expansion of hybrid perovskite inhibits halogen interstitial generation and enhances solar cell performance. *Nat. Commun.* **16**, 8591 (2025).
40. F. Xu, E. Aydin, I. Yavuz, C. Deger, E. Ugur, J. Liu, X. Zhang, A. Razzaq, L. Xu, M. Marengo, B. Vishal, A. Prasetio, A. Subbiah, A. Pininti, T. Allen, S. De Wolf, Stabilized perovskite phases enabling efficient perovskite/perovskite/silicon triple-junction solar cells. *Nat. Mater.* **25**, 259–266 (2026).
41. D. Gao, B. Li, X. Sun, Q. Liu, C. Zhang, L. Qian, Z. Yu, X. Li, X. Wu, B. Liu, N. Wang, F. Vanin, X. Xia, J. Gong, N. Li, X. C. Zeng, Z. Li, Z. Zhu, High-efficiency perovskite solar cells enabled by suppressing intermolecular aggregation in hole-selective contacts. *Nat. Photonics* **19**, 1070–1077 (2025).
42. Q. Tan, Z. Li, G. Luo, X. Zhang, B. Che, G. Chen, H. Gao, D. He, G. Ma, J. Wang, J. Xiu, H. Yi, T. Chen, Z. He, Inverted perovskite solar cells using dimethylacridine-based dopants. *Nature* **620**, 545–551 (2023).
43. X. Zheng, Z. Li, Y. Zhang, M. Chen, T. Liu, C. Xiao, D. Gao, J. B. Patel, D. Kuciauskas, A. Magomedov, R. A. Scheidt, X. Wang, S. P. Harvey, Z. Dai, C. Zhang, D. Morales, H. Pruett, B. M. Wieliczka, A. R. Kirmani, N. P. Padture, K. R. Graham, Y. Yan, M. K. Nazeeruddin, M. D. McGehee, Z. Zhu, J. M. Luther, Co-deposition of hole-selective contact and absorber for improving the processability of perovskite solar cells. *Nat. Energy* **8**, 462–472 (2023).
44. C. C. Stoumpos, C. D. Malliakas, M. G. Kanatzidis, Semiconducting tin and lead iodide perovskites with organic cations: Phase transitions, high mobilities, and near-infrared photoluminescent properties. *Inorg. Chem.* **52**, 9019–9038 (2013).

45. P. Jasinski, V. Petrovsky, T. Suzuki, H. U. Anderson, Impedance studies of diffusion phenomena and ionic and electronic conductivity of cerium oxide. *J. Electrochem. Soc.* **152**, J27 (2005).
46. M. Bag, L. A. Renna, R. Y. Adhikari, S. Karak, F. Liu, P. M. Lahti, T. P. Russell, M. T. Tuominen, D. Venkataraman, Kinetics of ion transport in perovskite active layers and its implications for active layer stability. *J. Am. Chem. Soc.* **137**, 13130–13137 (2015).
47. Z. Zhang, W. Chen, X. Jiang, J. Cao, H. Yang, H. Chen, F. Yang, Y. Shen, H. Yang, Q. Cheng, X. Chen, X. Tang, S. Kang, X. Ou, C. J. Brabec, Y. Li, Y. Li, Suppression of phase segregation in wide-bandgap perovskites with thiocyanate ions for perovskite/organic tandems with 25.06% efficiency. *Nat. Energy* **9**, 592–601 (2024).
48. Q. Jiang, J. Tong, Y. Xian, R. A. Kerner, S. P. Dunfield, C. Xiao, R. A. Scheidt, D. Kuciauskas, X. Wang, M. P. Hautzinger, R. Tirawat, M. C. Beard, D. P. Fenning, J. J. Berry, B. W. Larson, Y. Yan, K. Zhu, Surface reaction for efficient and stable inverted perovskite solar cells. *Nature* **611**, 278–283 (2022).
49. H. Zai, P. Yang, J. Su, R. Yin, R. Fan, Y. Wu, X. Zhu, Y. Ma, T. Zhou, W. Zhou, Y. Zhang, Z. Huang, Y. Jiang, N. Li, Y. Bai, C. Zhu, Z. Huang, J. Chang, Q. Chen, Y. Zhang, H. Zhou, Wafer-scale monolayer MoS_2 film integration for stable, efficient perovskite solar cells. *Science* **387**, 186–192 (2025).
50. J. Shi, Y. Li, Y. Li, D. Li, Y. Luo, H. Wu, Q. Meng, From ultrafast to ultraslow: Charge-carrier dynamics of perovskite solar cells. *Joule* **2**, 879–901 (2018).
51. D. Jiang, Z. Liu, J. Li, H. Cao, Y. Qian, Z. Ren, S. Zhang, Y. Qiu, C. Zhang, J. Wei, L. Yang, S. Yin, Non-laser and all-vapor-phase processed perovskite solar modules stabilized by naturally formed barrier layers. *Joule* **8**, 1161–1175 (2024).
52. Y. Qian, J. Li, H. Cao, Z. Ren, X. Dai, T. Huang, S. Zhang, Y. Qiu, L. Yang, S. Yin, Passivating perovskites in air via an alternating cation interlayer phase formed by benzylamine vapor fumigation. *Adv. Funct. Mater.* **33**, 2214731 (2023).
53. I. Zizak, The mySpot beamline at BESSY II. *J. Large-Scale Res. Facil. JLSRF* **2**, A102 (2016).
54. J. Kieffer, D. Karkoulis, PyFAI, a versatile library for azimuthal regrouping. *J. Phys. Conf. Ser.* **425**, 202012 (2013).
55. S. M. Park, M. Wei, J. Xu, H. R. Atapattu, F. T. Eickemeyer, K. Darabi, L. Grater, Y. Yang, C. Liu, S. Teale, B. Chen, H. Chen, T. Wang, L. Zeng, A. Maxwell, Z. Wang, K. R. Rao, Z. Cai, S. M. Zakeeruddin, J. T. Pham, C. M. Risko, A. Amassian, M. G. Kanatzidis, K. R. Graham, M. Grätzel, E. H. Sargent, Engineering ligand reactivity enables high-temperature operation of stable perovskite solar cells. *Science* **381**, 209–215 (2023).
56. S. Liu, T. Miao, J. Wang, Y. Zhang, R. Chen, X. Lei, W. Qin, Z. Zhu, L. Lu, Z. Chen, P. Cui, L. Li, M. Li, E. Xu, Y. Shen, S. C. Cho, S. U. Lee, S.-H. Cho, Z. Liu, W. Chen, N.-G. Park, Solvated-intermediate-driven surface transformation of lead halide perovskites. *Nat. Energy* **11**, 109–120 (2026).
57. G. Li, Z. Zhang, B. Agyei-Tuffour, L. Wu, T. W. Gries, K. Prashanthan, L. Frohloff, A. Musiienko, J. Li, R. Zhu, L. J. F. Hart, L. Wang, Z. Li, B. Hou, N. Koch, M. Saba, P. R. F. Barnes, J. Nelson, P. J. Dyson, M. K. Nazeeruddin, M. Li, A. Abate, Stabilizing high-efficiency perovskite solar cells via strategic interfacial contact engineering. *Nat. Photonics* **20**, 55–62 (2026).
58. Z. Zhang, R. Zhu, G. Li, Y. Tang, H. Wu, J. Zhao, J. Wu, T. W. Gries, A. Musiienko, S. Zuo, Z. Li, B. He, Z. Su, X. Gao, W. Zuo, B. Hou, J. Pascual, L. Sapienza, L. Wang, L.-L. Deng, Y. Jia, G. Li, P. J. Dyson, M. K. Nazeeruddin, M. Saliba, A. Abate, M. Li, Photoswitchable isomers to improve grain boundary resilience and perovskite solar cells stability under light cycling. *Nat. Energy* **11**, 623–632 (2026).
59. C. Fei, Y. Zhang, M. Wang, Y. Yang, X. Shi, S. Wang, H. Guo, C. Guo, H. Liu, M. Li, H. Gu, S. Barlow, W. You, M. Wang, S. R. Marder, J. Huang, Limiting phosphonic acid interlayer–perovskite reactivity to stabilize perovskite solar modules. *Science* **391**, eadz7969 (2026).
60. S. Sidhik, I. Metcalf, W. Li, T. Kodalle, C. J. Dolan, M. Khalili, J. Hou, F. Mandani, A. Torma, H. Zhang, R. Garai, J. Persaud, A. Marciel, I. A. Muro Puente, G. N. M. Reddy, A. Balvanz, M. A. Alam, C. Katan, E. Tsai, D. Ginger, D. P. Fenning, M. G. Kanatzidis, C. M. Sutter-Fella, J. Even, A. D. Mohite, Two-dimensional perovskite templates for durable, efficient formamidinium perovskite solar cells. *Science* **384**, 1227–1235 (2024).
61. J. Park, J. Kim, H.-S. Yun, M. J. Paik, E. Noh, H. J. Mun, M. G. Kim, T. J. Shin, S. I. Seok, Controlled growth of perovskite layers with volatile alkylammonium chlorides. *Nature* **616**, 724–730 (2023).
62. Z. Li, X. Sun, X. Zheng, B. Li, D. Gao, S. Zhang, X. Wu, S. Li, J. Gong, J. M. Luther, Z. Li, Z. Zhu, Stabilized hole-selective layer for high-performance inverted p-i-n perovskite solar cells. *Science* **382**, 284–289 (2023).
63. S. Yu, Z. Xiong, H. Zhou, Q. Zhang, Z. Wang, F. Ma, Z. Qu, Y. Zhao, X. Chu, X. Zhang, J. You, Homogenized NiO_x nanoparticles for improved hole transport in inverted perovskite solar cells. *Science* **382**, 1399–1404 (2023).
64. S. Sidhik, Y. Wang, M. De Siena, R. Asadpour, A. J. Torma, T. Terlier, K. Ho, W. Li, A. B. Puthirath, X. Shuai, A. Agrawal, B. Traore, M. Jones, R. Giridharagopal, P. M. Ajayan, J. Strzalka, D. S. Ginger, C. Katan, M. A. Alam, J. Even, M. G. Kanatzidis, A. D. Mohite, Deterministic fabrication of 3D/2D perovskite bilayer stacks for durable and efficient solar cells. *Science* **377**, 1425–1430 (2022).

Acknowledgments: We acknowledge the allocation of synchrotron radiation beamtime at mySpot BESSY II (HZB, Germany) and the BL02U2 Surface Diffraction Beamline at the Shanghai Synchrotron Radiation Facility (SSRF). We also acknowledge help from I. Zizak at mySpot beamline and from H. Bai from H.B. at Fuller | Kömmerling. **Funding:** This work was funded by the National Key R&D Program of China grant 2022YFB4200701 (S.Y. and J. Lian), the National Natural Science Foundation of China grant 61974103 (H.C.), the Key R&D Program of Shandong Province China grant 2024SFGC0103 (J. Li), the Tianjin Natural Science Foundation grant 24JCQNJC00960 (Q.Z.), and the Helmholtz Association [program-oriented funding phase IV, MTET Topic 1, Code: 38.01.04/Solar Technology Acceleration Platform (Solar TAP)] (U.W.P.).
Author contributions: Conceptualization: Z.R., J.D., and H.C. Methodology: Z.R., C.C., and J. Li. Software: Z.R. Validation: Z.R., C.C., and S.Y. Formal analysis: Z.R., H.C., C.C., J. Li, and Y.Q. Investigation: Z.R., Y.Q., C.C., J. Li, and S.Z. Resources: Z.R., H.C., C.C., U.W.P., and L.Y. Data curation: Z.R., C.C., and J. Li. Writing—original draft: Z.R. Writing—review and editing: Z.R., Y.Q., H.C., C.C., U.W.P., J. Li, and Q.Z. Visualization: Z.R., Y.Q., H.C., C.C., and Q.Z. Supervision: Z.R., H.C., J. Li, S.Y., and J. Lian. Project administration: C.C., J. Li, S.Y., and J. Lian. Funding acquisition: H.C., Q.Z., S.Y., and J. Lian. **Competing interests:** The authors declare that they have no competing interests. **Data, code, and materials availability:** All data and code needed to evaluate and reproduce the results in the paper are present in the paper and/or the Supplementary Materials. This study did not generate new materials.

Submitted 20 January 2026
Accepted 27 April 2026
Published 5 June 2026
10.1126/sciadv.aef6596

ScienceAdvances

Reactive reconstruction and embedded passivation of heterointerfaces for intrinsically stable perovskite photovoltaics

Zhixin Ren, Jike Ding, Yuan Qiu, Huanqi Cao, Cong Chen, Shifu Zhang, Ulrich Wilhelm Paetzold, Jinzhao Li, Qian Zhao, Liying Yang, Shougen Yin, and Jijian Lian

Sci. Adv. **12** (23), eaef6596. DOI: 10.1126/sciadv.aef6596

Science Advances (ISSN 2375-2548) is published by the American Association for the Advancement of Science. 1200 New York Avenue NW, Washington, DC 20005. The title *Science Advances* is a registered trademark of AAAS.